Artificial Organs

Development of a Magnetic Attachment Method for Bionic Eye Applications

*†Kate Fox, ‡§Hamish Meffin, **Owen Burns, ††Carla J. Abbott, ††Penelope J. Allen, ††Nicholas L. Opie, **Ceara McGowan, ††Jonathan Yeoh, *Arman Ahnood, ††Chi D. Luu, *Rosemary Cicione, **Alexia L. Saunders, **Michelle McPhedran, **Lisa Cardamone, **Joel Villalobos, *,**David J. Garrett, **David A. X. Nayagam, *,**Nicholas V. Apollo, *Kumaravelu Ganesan, **Mohit N. Shivdasani, *Alastair Stacey, *Mathilde Escudie, *Samantha Lichter, **Robert K. Shepherd, and *Steven Prawer

*School of Physics; ‡Department of Electrical and Electronic Engineering, University of Melbourne; †School of Aerospace, Mechanical and Manufacturing Engineering, RMIT University; §National Vision Research Institute, Australian College of Optometry; **The Bionics Institute; and ††Centre for Eye Research Australia (CERA) Royal Victorian Eye and Ear Hospital, Melbourne, Victoria, Australia

Abstract: Successful visual prostheses require stable, long-term attachment. Epiretinal prostheses, in particular, require attachment methods to fix the prosthesis onto the retina. The most common method is fixation with a retinal tack; however, tacks cause retinal trauma, and surgical proficiency is important to ensure optimal placement of the prosthesis near the macula. Accordingly, alternate attachment methods are required. In this study, we detail a novel method of magnetic attachment for an epiretinal prosthesis using two prostheses components positioned on opposing sides of the retina. The magnetic attachment technique was piloted in a feline animal model (chronic, nonrecovery implantation). We also detail a new method to reliably control the magnet coupling force using heat. It was found that the force exerted upon the tissue that separates the two components could be minimized as the measured force is proportionately smaller at the working distance. We thus detail, for the first time, a surgical method using customized magnets to position and affix an epiretinal prosthesis on the retina. The position of the epiretinal prosthesis is reliable, and its location on the retina is accurately controlled by the placement of a secondary magnet in the suprachoroidal location. The electrode position above the retina is less than 50 microns at the center of the device, although there were pressure points seen at the two edges due to curvature misalignment. The degree of retinal compression found in this study was unacceptably high; nevertheless, the normal structure of the retina remained intact under the electrodes. **Key Words:** Magnet—Bionic eye—Attachment—Retina.

In line with advances in the field of bionic eye research, the development of an appropriate technique to attach and secure retinal implants is essential to harvest the full potential of implanted devices. At present, the surgical approaches for implanting a retinal prosthesis can be classified in two means: (i) mechanical anchoring of the implant on the epiretinal surface or (ii) implantation of the implant in the mechanically stable position between retinal layers (e.g., beneath the retina [subretinal] or within the suprachoroidal space). The placement of the implant distal from the retinal neurons, as is the case for the suprachoroidal implant, limits the best achievable visual acuity of the device, hence restricting the resolution of the implant. Conversely, epiretinal positioning allows placement of the device closer to the retinal neurons (retinal ganglion cells), thus opening the possibility of achieving high acuity vision (Fig. 1) (2). From the surgical point of view, the epiretinal location is a less intrusive means of implant placement than the subretinal location. The

doi:10.1111/aor.12582

Received January 2015; revised May 2015.

Address correspondence and reprint requests to Kate Fox, School of Aerospace, Mechanical and Manufacturing Engineering, RMIT University, Carlton, Vic. 3056, Australia. E-mail: kate.fox@rmit.edu.au

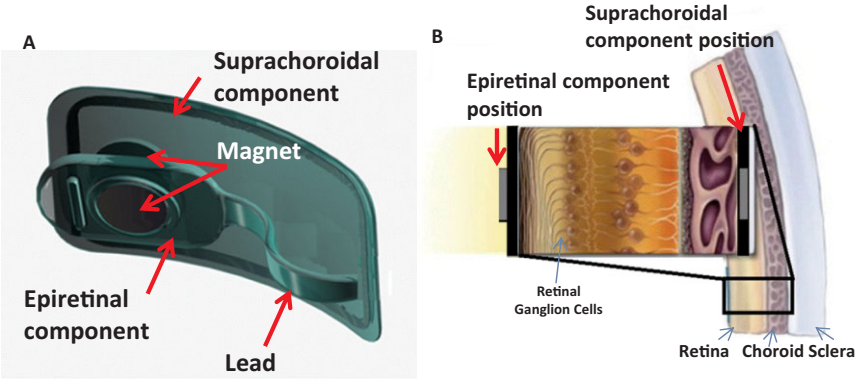

FIG. 1. (A) A diagram of the magnetic attachment technique showing one NdFeB magnet on the back of an epiretinally positioned component and a second magnet positioned in the suprachoroidal space. (B) The anatomical positions of the two prosthesis components (modified from Shepherd et al. [1] with permission from the publisher).

epiretinal approach, however, requires permanent mechanical anchoring to secure the implant in close proximity to the retina (3–5) near the posterior pole of the eye.

Permanent magnets are common as implantable device elements. Rare earth magnets made of special alloys such as neodymium-iron-boron (NdFeB) are commonly used in the external coil of cochlear implants (6,7), orthopedic fixation (8), and in dental applications (9,10). The main advantage of rare earth magnets is that they have a large magnetic flux density relative to its size and do not lose their magnetic strength over time. Common limitations to the use of NdFeB as a biomedical fixation tool, however, include lack of biocompatibility, degradation particularly in chloride rich environments (9,11,12) (likely linked to the high content of the highly electrochemically active Nd (13)), and the inability for magnet-containing implants to be used in magnetic resonance imaging (14,15). In order to prevent degradation, NdFeB magnets have been coated in materials such as parylene (16) and silane (13) which have proven to provide the necessary resistance to corrosion and physiological isolation. Magnets, however, have not been attempted as an epiretinal attachment method.

At present, for epiretinal prostheses, two mechanical anchoring techniques have been studied, tacks (4,17–23) and glues (24), with only tacks progressing into clinical trials. The tacks are designed to be sharp arrow-like structures that penetrate the implant, retina, and choroid before the head of the tack is stabilized either within or through the sclera. By design, the retinal tack introduces significant trauma onto the retinal neurons including the ganglion cells that the device is designed to stimulate. Long-term implantation of tacks by other groups have shown mixed results (3,4,18,21,23,25) with reports of contained damage zones (4,25) but also of gliosis (18), tack extrusion (17), and trauma (21). Concerns exist as to the ability to remove tacks should the device malfunction. Recent work by de Juan et al. (4) showed that tack extraction from an epiretinally located implant can occur without complications in degenerative retinas after long-term implantation (from 14 to 19 months). However, both placement and removal of tacks require a high level of surgical skills (precise intraoperative device placement and then the act of retinal tacking with an external tacking tool).

Here, we present a novel concept, using magnets for attachment of an epiretinal prosthesis. We use a two component prostheses whereby we place a backing magnet in a highly stable position, the suprachoroidal space, and the primary magnet on the back of the epiretinally positioned electrode array. Given the importance of placing the device as close as possible to the macula (26), the suprachoroidal component is implanted prior to the epiretinal component. Therefore, with the suprachoroidal component, we can control the location of the epiretinal device on the retina which is not easily achieved when using tacks. Images of the epiretinal and suprachoroidal components and their anatomical location in the retina are provided in Fig. 1. The device has a 25-strand platinum lead with a moulded elbow to aid in positioning the lead through the scleral wound. The suprachoroidal component has two Dacron patches to provide mechanical stability by enabling suturing of the suprachoroidal component onto the sclera.

The purpose of this study was to determine the feasibility of using a magnet as an attachment method for an epiretinal implant. We outline a method to customize the magnets using heat to control magnetic coupling force in order to reduce pressure on retinal tissue. Furthermore, we pilot a novel surgical technique for epiretinal implants using a magnetically coupled two-part device. The effectiveness of using a pair of magnets to couple a medical device against the retina is investigated using

short-term and long-term in vivo assessments of devices implanted in a feline model.

MATERIALS AND METHODS

Control of magnet strength

Rare earth neodymium-iron-boron (NdFeB) magnet discs (SuperMagnetMan, Birmingham, AL, USA) with a diameter of 3 mm and thickness of 0.3 mm were selected to test the coupling force between magnet pairs over a range of anatomically relevant separation distances. Magnetic flux density was measured using a Gaussmeter (AlphaLab Inc, Pittsburgh, PA, USA). The separation between magnets was achieved with 3D-printed acrylonitrile butadiene styrene spacers to ensure repeatable measurements. The coupling force measured between magnet pairs was calculated using an in-house developed test that applied a set weight to one of a pair of coupled magnets to induce decoupling under gravitational force. In order to induce weaker magnet pairings, individual magnets were thermally weakened by placing them on a digital hotplate and measuring the magnetic flux density with a Gaussmeter after exposure to set temperature points (25–150°C) for 1 min. The coupling force corresponding to the magnetic flux density of each magnet pairs was normalized with respect to the unmodified (nonheated) magnet pair. In other words, 100% represents the combined magnetic flux density of two unmodified diameter 3×0.3 mm magnets.

Stability of magnet coatings

Nonbiocompatible elements in NdFeB magnets make them unsuitable for in vivo implantation. The issue was addressed by coating the magnets with biocompatible films, either thin metallic or polymer coatings. Titanium and gold coatings were applied using electron beam evaporation (Thermonics, Inc., Mansfield, MA, USA) at a rate of 0.2 Å/min and a thickness of 100 and 20 nm, respectively. Sputter-coated gold coatings were applied using a sputter coater (SPI Supplies, West Chester, PA, USA) at a rate of 3 Å/sec for an estimated thickness of 80 nm. Parylene C-coated magnets were sourced from SuperMagnetMan and had a coating thickness of 8 μm. Magnetic flux density was recorded after coating using a handheld Gaussmeter. The ability of coated NdFeB magnets to resist corrosion in the biological environment was assessed by an immersion test in which the magnets were soaked in a highly corrosive 70% HNO_3 solution, which readily etches the magnet but does not attack the biocompatible coating (27–29). The ability of coated magnets to resist corrosion was assessed by visual inspection of the magnets after soaking for 1 min, 1 h, and 1 day.

Suitability for securing a retinal prosthesis

Suitability of the NdFeB magnets as a method of attachment for epiretinal implant was assessed using a combination of benchtop and in vivo assessments. The implant consists of two separate implantable components: (i) an epiretinal silicone substrate with an embedded magnet and diamond electrode array; and (ii) a suprachoroidal silicone substrate with an embedded magnet (Fig. 1A). The silicone used was 30 durometer and moulded using an external mould derived from analyzing a series of optical coherence tomography (OCT) scans in both the lateral and longitudinal direction across the retina. The embedded magnets were parylene coated, and the diamond device was 800 μm thick (30). The two components are held (coupled) across the tissue between them (Fig. 1B). It is important to note that the suprachoroidal component was implanted first and therefore dictates the position of the epiretinal component.

Surgical validation

Validation and optimization of our surgical procedures were approved by the Royal Victorian Eye and Ear Hospital Animal Research Ethics Committee in compliance with the "Australian code of practice for the care and use of animals for scientific purposes" (7th Edition, 2004), the "Principles of laboratory animal care" (NIH publication No. 85-23, revised 1985), and the ARVO standards for use of animals in ophthalmic research. In vivo device placement required a two-part unilateral surgical procedure with an initial surgery to implant the suprachoroidal component and a subsequent surgery to attach the epiretinal component. To validate our surgical approach, feline subjects were used as an in vivo model. Normally sighted adult cats weighing 3.0–6.4 kg were anesthetized with an initial subcutaneous injection of xylazine (2 mg/kg) and a subcutaneous injection of ketamine (20 mg/kg). Animals were separated into two studies, with 22 animals used in nonrecovery studies for surgical optimization and three animals used in chronic studies to assess the long-term mechanical stability of the magnets. In the nonrecovery studies, anesthesia in animals was maintained using a continuous, intravenous infusion of sodium pentobarbitone (60 mg/mL, 1:6 dilution), and Hartmann's solution (sodium lactate, 1.5 mg/mL/h) was supplied for fluid replacement (31). In the chronic studies, anesthesia was maintained using isofluorane (initial dose 0.5% and increased

according to respiratory activity). Body temperature was monitored and maintained at 37.0 ± 1.0°C using a heating pad. Respiration rate and end-tidal CO_2 levels were monitored using a capnograph connected to an endotracheal tube. Pupils were dilated using a combination of 0.5% tropicamide, 1% atropine sulphate, and 10% phenylephrine hydrochloride. Eyes were protected against dehydration during the experiment with hypromellose gel.

The suprachroidal surgery was performed in accordance with methods described previously (32,33). Briefly, both a lateral canthotomy and a temporal conjunctival peritomy were performed. Bipolar diathermy was applied to the sclera in the temporal quadrant parallel to the limbus to reduce bleeding during surgery. A 9-mm scleral incision, 5-mm posterior and parallel to the limbus was then made in the area treated with diathermy to expose the choroid. A pocket was opened in between the sclera and the choroid using an angled crescent blade. The suprachoroidal space was then dissected with a lens glide, and the implant was inserted approximately 15 mm into the suprachoroidal space. The wound was closed with 5/0 nylon and 8/0 nylon sutures (Johnson & Johnson Medical, Sydney, NSW, Australia), and the suprachoroidal component was then stabilized by passing two of the sutures through a Dacron patch on the anterior end of the component. A wide-angle quadraspheric lens (Volk, Mentor, OH, USA) was placed on the eye to check the position of the suprachoroidal component, and the component was repositioned as required.

Following the dissection of the nictitating membrane, the conjunctival peritomy was completed. To perform the epiretinal surgery, a 20-G three-port pars plana approach was made with the infusion line placed 4 mm from the limbus on the temporal side. Nasal and superior sclerotomies were made for insertion of the light source and outcome, respectively. A complete lensectomy and vitrectomy were performed using a contact lens to visualize the posterior segment. Adrenalin was administered as required (0.25–0.5 mL) to dilate the pupil if miosis occurred. Following removal of the lens and vitreous gel, a 6-mm incision was created 5 mm from the limbus through which the epiretinal component was inserted, positioned, and attached. Scleral wounds were sealed using either histoacryl (B. Braun, Sydney, NSW, Australia) or photo-cross-linked fibrinogen glue as detailed in Elvin et al. (34). To assist in the sealing of the wound, the eye was in some instances filled with air. The eye was then refilled with either balanced salt solution or silicone oil to keep the eye inflated and to assist with spectral domain OCT retinal imaging (Spectralis Heidelberg Engineering GmbH, Heidelberg, Germany). For the nonrecovery studies, both epiretinal and suprachoroidal surgeries were performed on the same day. For the chronic study, the epiretinal surgery was performed 14 days after the suprachoroidal surgery to allow the retina and choroidal edema to recover between surgeries.

Chronic implantation

For the chronic implantation studies (≤6 weeks), two cats were unilaterally implanted with the epiretinal and suprachoroidal magnet components. The cats were allowed to recover from surgery and move freely. The animals were overdosed and perfused after 6 (subject 1) and 5 weeks (subject 2). Subject 2 was terminated early due to a breakdown of the scleral wound. Extracted eye tissue was postfixed using histological techniques developed previously (35). Retinal tissue was embedded in agar (4% w/v; Sigma Aldrich, Sydney, NSW, Australia). Tissue was processed, paraffin embedded, cut into serial sections (5 μm thickness), and stained with hematoxylin and eosin.

Retinal images were taken fortnightly following the surgery. Fundus photographs were taken with a Topcon TRX 50DX Fundus Camera (Topcon Medical Systems, Santa Clara, CA, USA) to assess gross pathological damage and the position of the device in situ. Spectral domain OCT was also used to assess the distance of the epiretinal component from the retina and to evaluate any retina damage that may have occurred due to implantation of the device. A fluorescein angiogram was performed prior to termination to detail retinal and choroidal blood vessel flow. A bolus of fluorescein sodium (20 mg/kg, Retinofluor, Phebra) was injected intravenously, and serial retinal photographs were taken in fluorescence mode for 30 min.

RESULTS

Determination of magnet parameters

Figure 2 presents the results of heat treatment of NdFeB magnets on magnetic strength. Figure 2A shows that heating the magnets for 1 min to temperatures between 25 and 150°C resulted in demagnetization of the magnets that followed a semi-linear trend. In addition, re-testing these magnets 1 week postheat treatment indicated that the drop in the magnet strength induced by heat treatment is permanent. Figure 2B shows a comparison of the force exerted between the magnets relative to the

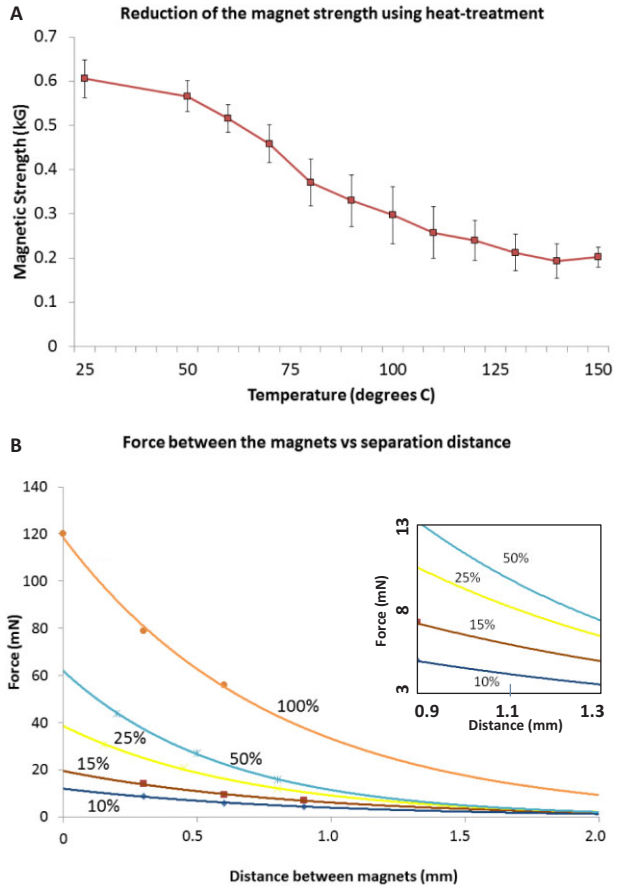

FIG. 2. (A) The effect on magnetic flux density of heating the NdFeB magnet from 25 to 150°C for 1 min at each temperature point. Error bars represent the standard deviation from the mean. (B) The force exerted by two paired 3×0.3 mm magnets after reducing the magnetic flux density of individual magnets with the inset highlighting the variation of the force between the paired magnets over the expected separation of the magnets when used in the proposed retinal prosthesis. One hundred percent represents a pair of as-received magnets and 50% a pair of magnets customized to have their combined flux density to be half of the as-received magnet pair.

separation between the magnet pair. Irrespective of magnetic strength, coupling between NdFeB magnets was negligible when separated by more than 2.5 mm. The distance between the suprachoroidal magnet and the epiretinal magnet is typically 0.9–1.3 mm (owing to the thickness of the epiretinal component and the tissue between the two components). The magnetic coupling forces for this range of separation are shown in the inset of Fig. 2B. The inset highlights that variations in the retina-choroidal tissue thickness will have a limited effect on the tissue force as over the expected working distance, the variance in the force exerted on the tissue is limited to 5 mN at 50% and 1 mN at 10% magnetic flux density. The high coupling force of the as-received (100%) magnet pair precludes its use in such a delicate position as upon the retina, and thus, heat modification of the magnets is necessary to reduce the force exerted on the retinal tissue. It is unknown as to the maximum force the retina can withstand; however, an estimate of the maximum force that the retina can sustain may be obtained by considering glaucoma patients who report retinal damage when intraocular pressure is increased by 6–33 mm Hg (36). This pressure is spread across a larger area than our device; however, using this value, it is apparent that the magnetic strength needs to be reduced to at least 50% of its as-received value which can be achieved by heating the magnet to 100°C.

Resistance to environmental conditions

Figure 3 shows a comparison of NdFeB magnets coated with a variety of common coating materials to determine whether these coatings affect magnetic flux density (Fig. 3A) and protect the magnet from corrosion (Fig. 3B). Evaporating titanium and gold

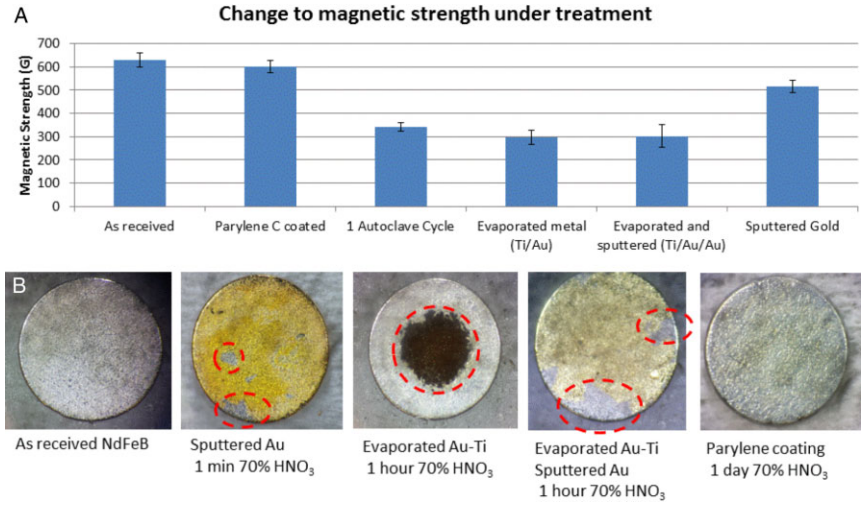

FIG. 3. The effect of coating NdFeB magnets on magnetic flux density and corrosion. (A) The change of the magnetic field strength as measured by a handheld gaussmeter under a variety of coatings and treatments (error bars represent the standard deviation from the mean). (B) Representative images of the magnets after they were soaked in a 70% HNO_3. After 1 day, only the parylene C-coated magnets were resistant to the HNO_3. The HNO_3 soak test for metallic and polymer coatings was repeated for $n = 3$ samples and the failure points in each image highlighted by a dashed ring.

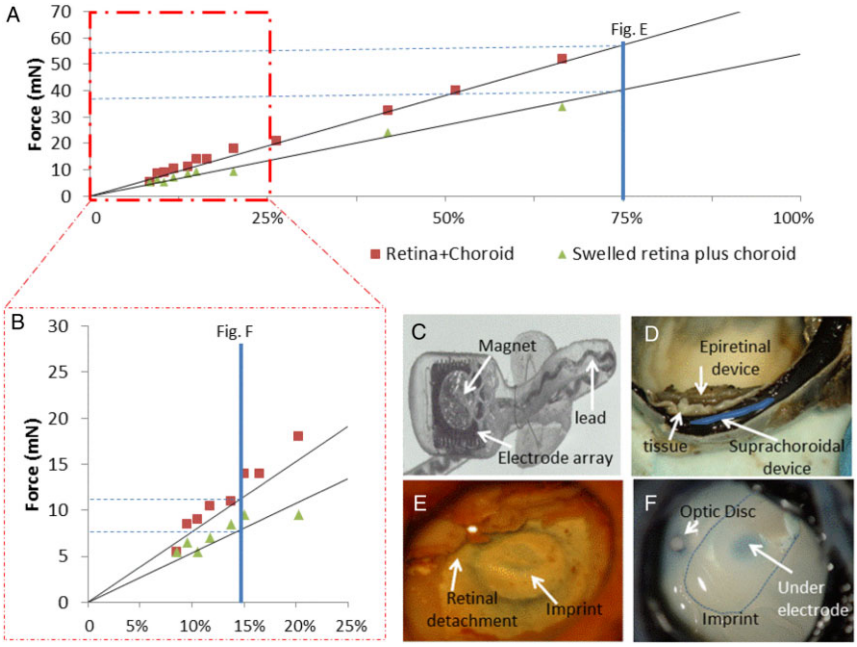

FIG. 4. Surgical optimization from nonrecovery surgery (6 h implantation). (A) The variety of magnet combinations attempted in vivo. The forces between the components were calculated as per the linear lines representing retina plus choroid (0.4 mm, red squares) and swollen tissue (0.6 mm, green triangles). The device strength is represented as a % of the combined magnetic flux density of a pair of prostheses embedded as-received NdFeB magnets. The vertical blue lines represent the magnet combination used in the two studies shown in *E* and *F*; (B) an inset of (A); (C) the epiretinal component of the device used for the studies; (D) vertical postmortem cross-sectional image through a posterior eyecup showing the anatomical positioning of the two components; the suprachoroidal component has been colored to facilitate viewing. (E) A postmortem image of the retinal surface after 38–55-mN force showing a clear circular imprint of the center of the epiretinal component likely introduced by compression of the underlying retina by the epiretinal component the under magnetic force and (F) after 8–11 mN force with the position of the component highlighted in blue dashes showing a thinning of the retina beneath the device where the electrode array would have been positioned.

films onto the magnets using electron beam evaporation resulted in a loss of over 50% of the magnetic field due to the temperature increase of the magnets during the deposition of the vaporized metal from the crucible. Given the low Curie temperature of NdFeB magnets, using an autoclave to sterilize the magnets for surgical application resulted in a reduction in magnetic flux density, as expected. Parylene coating did not cause any change to the magnetic flux density. Figure 3B shows representative images of coated magnets that were soaked in 70% HNO_3; the highlighted dashed regions indicate failures in the coating material, likely due to pin holes present in the coated materials. HNO_3 was chosen to test the integrity of coating materials as it is known to readily dissolve nickel, and thus, any nickel exposed from the NdFeB magnet due to failures in the coating material will react with the solution. The as received NdFeB magnets dissolved in less than 1 min ($n = 10$ samples) when exposed to this solution. When soaked in HNO_3, delamination was observed in sputtered Au samples, as evidenced by gold film in the nitric acid solution, due to the resistance of gold to HNO_3. Delamination occurred in these samples after soaking from 1 min in HNO_3 and magnets dissolved completely within 1 h. The evaporated Au/Ti coating was observed to fail and expose neodymium after soaking for 1 h. Adding a sputtered Au coating to the evaporated Au/Ti coating did not protect the magnets from corrosion; rather, it extended the time before the magnet dissolved. The parylene-coated magnets, however, were resistant to HNO_3 and after 1 day of HNO_3 soaking remained undamaged with no visual failure points observed.

Optimization of magnet selection for in vivo applications

Preliminary short-term in vivo studies (nonrecovery surgery with an implantation time of 6 h) were undertaken to determine the optimal magnet force that the retina could withstand without causing retinal trauma. A total of 22 surgeries were performed. Figure 4A,B shows the in vivo measurement of the force exerted between the suprachoroidal and epiretinal components (separated by estimated tissue thicknesses of 400–600 µm, Fig. 4D), and thus, the force expected to be exerted by the magnets on the retina and the choroid. The expected force typically

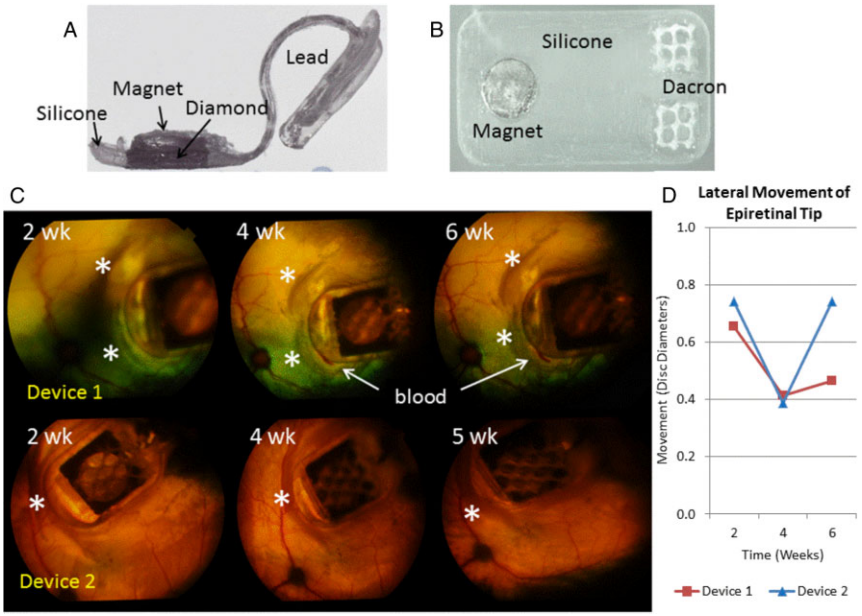

FIG. 5. *A* and *B* show the epiretinal and suprachoroidal magnet components used for the chronic implantation, respectively. *C* shows ocular fundus images of the implanted epiretinal component at three follow-up time points: 2 weeks, 4 weeks, and a final image prior to termination. Asterisks indicate retinal folding, which is seen from immediately postsurgery and changes minimally over the follow-up period, suggesting good mechanical stability. *D* shows the measured lateral movement of the tip of the epiretinal component relative to a photograph immediately postsurgery. The average movement of 0.5 (device 1) and 0.6 (device 2) optic disc diameters is minimal, again indicating good mechanical stability of the implanted devices.

ranged between 4 and 20 mN at the tissue interface. Figure 4E,F show images of the retina following implantation and subsequent removal of two devices whose coupling forces were chosen at the extremes of magnetic strength. The forces at the tissue interface were in the range of 38–55 mN for the strong device coupling (75% of the as received magnet strength) and 8–11 mN for the weaker device coupling (15% of the as received magnet strength). As can be seen from Fig. 4E, when device components are strongly coupled, there is a resulting impression of the epiretinal component on the retinal tissue. The imprinted ring is a reflection of the recessed nature of the center of the epiretinal component where the diamond electrodes are positioned. This trauma to the retina was not apparent in the surgery where device coupling was weaker (Fig. 4F). Subsequently, long-term studies to assess device stability proceeded with the weaker device coupling.

To assess the long-term stability of the magnetic attachment method, two chronic implantation surgeries (6 weeks) were undertaken (plus a pilot that is not reported here, see Methods). Based on the results of the nonrecovery in vivo study, the magnets used in the chronic devices were modified to exert approximately 12 mN of force at the 400 µm-thick tissue interface, which is equivalent to a minimum pressure of 2.82 mm Hg. Figure 5C shows ocular fundus images of the devices taken throughout the chronic study (weeks 2 and 4, and at termination). The fundus images show that in both free-roaming cats, the devices remained coupled for the duration of the implantation. However, retinal folding was observed around the silicone substrate of the epiretinal component particularly at the nasal end (indicated by the asterisks in Fig. 5C). The folding occurred during surgical implantation and appears consistently in each of the follow-up images. It is believed that this folding is due to a misalignment in shape between the silicone substrate and the contour of the eye.

The location of the tip (distal end) of the epiretinal component was compared in fundus images to asses if there was any movement of the device during the chronic study period. Minor movement was observed in device 1 (≤0.5 optic disc diameters, see Fig. 5D). However, this is approximately equivalent to the inherent measurement noise with this technique due to the retina being a curved surface. This is further supported by the stability in the location of the retinal folds in the follow-up fundus images and postmortem data (Fig. 7) where the imprint of the epiretinal component on the retina and absence of retinal tears indicated that the device did not drag across the retina. Mean movement of device 2 was observed to be 0.6 optic disc diameters (Fig. 5D). However, postmortem analysis revealed that the retinal fold at the distal end had increased and folded over the tip of the epiretinal component; therefore, the movement was calculated to be 0.7 optic disc diameters. This slight movement in the nasal direction is thought to be due to a breakdown of the scleral wound (and also the reason why the study did not complete the anticipated 6-week mark) which led to movement of the epiretinal component lead in the wound.

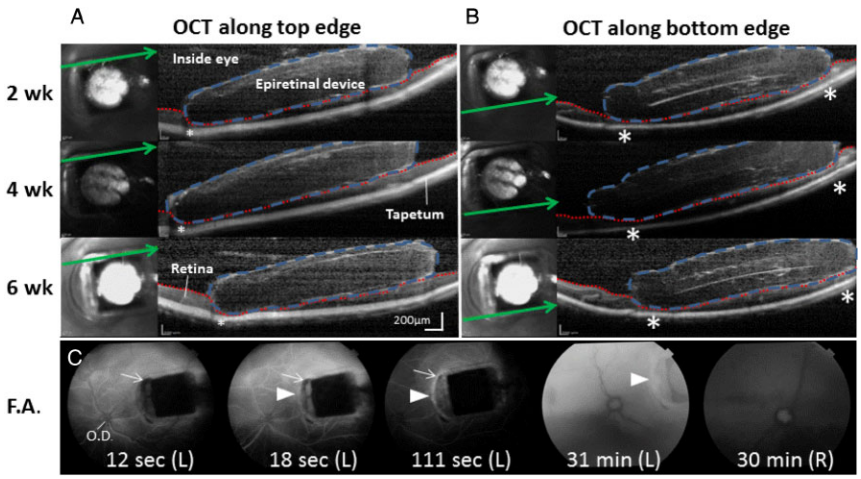

FIG. 6. (A) Representative OCT B-scan images through the top (superior) edge of device 1 and the accompanying infrared images to show the position of the B-scan relative to the epiretinal component position (green arrow). The outline of the epiretinal component is highlighted with blue dashes, and the top surface of the retina (inner limiting membrane) is shown with red dots. (B) Representative OCT B-scan images through the bottom (inferior) edge of device 1 with accompanying infrared images to show the B-scan position. Both top and bottom OCT scans indicate a mismatch in the conformity of the device with the underlying retina with pressure points at the temporal (left) and nasal (right) epiretinal component edges (shown with asterisks) but a good alignment between the central electrode sections. (C) Fluorescein angiogram of the retinal blood flow 6 weeks after device 1 was implanted. Results indicate that the pressure points induced by the shape mismatch result in a restriction of blood flow beneath the epiretinal component. This is evidenced by both reduced flow (dark patch) under the silicon at early time points (white arrows) and also by a bright rim (arrowheads) suggesting the blood pools around the epiretinal component due to the pressure points. At 30 min, there is some generalized vascular leakage in the implanted eye (L) compared with the nonimplanted eye (R), indicating some blood flow disruption. Scale in *A* applies to *B*. O.D., optic disc; L, left eye; R, right eye; wk, week.

Figure 6 shows representative OCT images through the superior (Fig. 6A) and inferior (Fig. 6B) edges of device 1. From these scans, the gap between the retina and diamond electrode array at the center of the epiretinal component was estimated to be less than 50 μm. The edges of the silicone substrate are, however, misaligned with respect to the retina and caused compression of the retina. The compression of the retina at the edges of the silicone substrate appears to increase over time, and retinal erosion can be seen. A similar result was seen for device 2; the gap between the retina and diamond electrode array was less than 25 μm (data not shown), and compression of the retina was also seen beneath the edges of the silicone substrate. Fig. 6C shows a fluorescein angiogram of retinal blood flow taken at the end of the chronic study with device 1. The angiogram indicates that blood flow beneath the epiretinal component is impeded, thereby further confirming the presence of compression trauma seen in the OCT images. Further, there is greater filling and leakage than normal in the regions adjacent to the compressed area. The general vascular incompetence is more widespread in the implanted eye than the fellow nonimplanted eye, although this is somewhat expected at 6 weeks postvitrectomy (37).

Figure 7A shows a postmortem image of device 1 in situ in the posterior eyecup. The postmortem dissection revealed that the tip of the silicone substrate of the epiretinal component was positioned at *area centralis*. Accordingly, the electrodes were temporal to the *area centralis*. Following removal of the epiretinal component (Fig. 7B), it was evident that the device made contact with the retina, particularly at the distal and proximal ends. This contact was not evident with devices in the nonrecovery studies that exerted similar forces at the tissue interface (Fig. 4C at 11 mN compared with 12 mN here). Pressure forces due to the mismatch between the contour of the epiretinal component and retina, particularly at the tip and lead ends of the component, resulted in retinal compression that was able to be observed during the longer, 6-week implantation time. Less compression was observed in the retina underlying the diamond electrode array owing to the recess of the electrodes within the silicone substrate. Figure 7C shows the histology of the eye used for device 1, including the retina beneath the implant. There was severe retinal compression of the inner retinal layers (outer nuclear layer, inner plexiform layer, nerve fiber layer, ganglion cell layer) beneath the magnet and a retinal fold beside the edge of the device. The compression in this region likely led to reactive retinal ganglion cells. The altered morphology of these cells would be expected to impede their normal function. These results suggest that the retina could

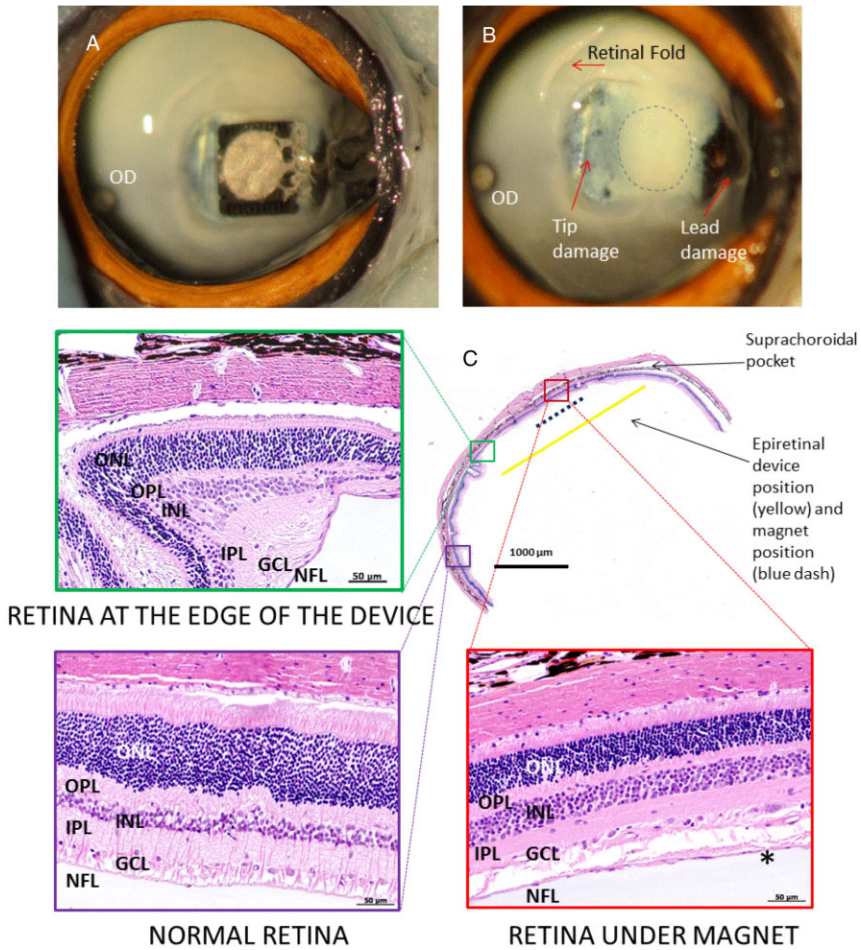

FIG. 7. Dissection and histological images of the eye used for device 1 in the chronic implantation study. (A) Device 1 in position and (B) the underlying retina postremoval of the device. (C) Histology of the retina for device 1: assessing the retina beneath the magnet and the retina at the edge of the device compared with the retina peripheral to the implant site. There was retinal compression beneath the magnet and at the edge of the device (comparing the plexiform layers [IPL] and cells in the ganglion cell layer [GCL] to the normal retinal architecture image). The ganglion cells are reactive, which would be expected to affect the normal functioning of these cells. Artifactual nerve fiber layer detachment indicated by asterisk (*). NFL, nerve fiber layer; GCL, ganglion cell layer; IPL, inner plexiform layer; INL, inner nuclear layer; OPL, outer plexiform layer; ONL, outer nuclear layer. Scale bar main image: 1000 µm; scale bar magnified images: 50 µm.

not withstand the mechanical forces between the coupled suprachoroidal and epiretinal magnets. Positively, there was no retinal detachment or hemorrhage, and the retinal cell layers remained organized, and thus, we have not, after 6 weeks, seen erosion or amelioration of the retina beneath the magnet as seen in the gross dissection where the pressure points induced by the edges of the epiretinal device have clearly eroded the retina (Fig. 7C "edge of the device").

Limitations of the study

The study performed here was not without limitations. The results are dominated by both controllable intrinsic factors (coupling force of the attachment) and also by extrinsic factors (surgical proficiency, lead forces). Numerous obstacles and difficulties arose within this study such as a delayed surgical complication ($N = 1$) and retinal injuries ($N = 2$). The time course of 5–6 weeks of this study, although optimized for short-term device stability, may have masked the long-term efficacy of the mismatched contour of the device relative to the contour of the underlying retinal tissue, particularly under magnetic compression. As a consequence the length of implantation and the small cohort size ($N = 2$) makes it difficult to draw finite conclusions in this study regarding the viability of the magnetic attachment method.

DISCUSSION

When designing a magnetic attachment strategy for a retinal prosthesis, it is crucial to understand the biological environment in which the magnets need to be positioned. Given that the backing magnet must be anatomically positioned behind the retina, there exist only two suitable locations in which it can be placed, in the suprachoroidal space or in the episcleral position. Here, we have selected the suprachoroidal position due to its known mechanical stability as a location for implants (1) and its success as the location of Bionic Vision Australia's first generation prosthesis (32). We showed that the shape and size of the first generation suprachoroidal device

minimized retinal trauma (32,38). Accordingly, the magnets to be used in the suprachoroidal component of the retinal prosthesis were selected to fit within the same substrate as the Bionic Vision Australia first-generation prosthesis. In Fig. 2A, we illustrated a reliable technique to demagnetize the NdFeB magnets in order to reduce their magnetic flux density. It is essential that we control the field strength of the magnets and the forces exerted between magnet pairs to ameliorate damage to the tissue placed between them. NdFeB magnets are known to demagnetize under heat with the Curie point for these magnets reported by the supplier to be approximately 80°C. This therefore precludes the use of autoclave sterilization of the magnets (commonly performed at 120°C). The magnetic force exerted at the tissue interface can be tailored using heat treatment and given knowledge of the magnetic field strength at the working distance. When considering that the epiretinal and suprachoroidal magnets would be separated by a minimum of 1 mm due to the thicknesses of the prostheses and tissue located between them, the optimized magnets thus offer minimal tissue compression force at the working distance (particularly postheat treatment). At the working distance, the retina-choroid tissue thickness variations have an increasingly lessened range of compression forces that may be exerted at the tissue interface (<13 mN).

It is critical that any material used in vivo is biocompatible and resistant to corrosion. NdFeB is not considered to be biocompatible owing to its high content of Nd which readily corrodes in chloride rich environments (16). Pin holes in secondary coatings are a major culprit of any coating failures (39). Unfortunately, it is highly difficult to locate these pin holes using visual inspection techniques. However, given that 70% HNO_3 readily dissolves NdFeB magnets, we can use this solution to test for failures in secondary coatings. Testing the coated magnets using 70% HNO_3 showed that only parylene was capable of protecting the underlying NdFeB magnet; all other samples corroded within an hour of nitric acid exposure. This is unsurprising, given that parylene has a reputation for providing a biostable, pin hole-free coating while also being highly resistant to corrosive environments (40). The failure mechanism in the metallic coatings which were tested was considered to be a direct result of the electron beam evaporation process that allowed only one side of the magnet to be coated with the desired metal at a time. Therefore, there is an obvious weak point at the interface between the two different coating layers.

After assessing the magnets on the bench for coating integrity and coupling force, it was essential that the in vivo characteristics were studied. Initial experiments to optimize a stable, low-force implant for chronic implantation were undertaken by placing a magnet on the back of the diamond capsule, and a second in a silicone substrate in the suprachoroidal space for 6 h (non-recovery) to determine the force that the retina can at least, temporarily, withstand. The key criteria for successful implementation of the magnets were twofold: (i) capacity to position and secure the device and (ii) avoid trauma to the retina. Accordingly, the short-term implantation surgeries were done at two ends of the magnetic coupling spectrum, one with a strong magnet pairing (75% of as received strength, expected force between the magnets of 38–55 mN) and 21 surgeries with weak magnet pairings (10–20%, 5–15 mN) to determine whether the magnets met the two key criteria. As the devices were implanted for less than a day, the analysis of magnet pairing was restricted to gross assessment techniques such as visual inspection during surgery to confirm positioning and inspection for tissue damage postfixation. Although the visual inspection of the fixed eye offers a gross assessment of device conformity and is subject to postfixation-induced artifact, it is a successful tool to perform an initial assessment of the magnetic attachment technique. When the force between magnet pairs was 5–15 mN, the impression of the epiretinal component on the retinal tissue that was seen with strong magnet pairings was not evident suggesting that this range of forces may be tolerated by the retinal tissue. However, to assess this further, a longer surgical implantation was required.

The chronically implanted prostheses exerted a force of approximately 12 mN (pressure = 2.82 mm Hg) at the tissue interface. This force was selected from the findings of the short-term implantation surgeries. Viewing the devices using both cross-sectional OCT and fundus imaging, retinal folding and damage were routinely seen across the 6-week implantation time suggesting that the devices were exerting a force on the retinal tissue beneath that may be unsuitable for long-term implantation. The folding was consistent across the implantation period, suggesting that most of the damage occurs within the first 2 weeks of implantation, and is thought to be linked to a mismatch between the curvature of the silicone substrate and eye. Minor device movement was seen; however, this was in line with the results reported for suprachoroidal device implantation (32,38) in which the device undergoes minor migration up to 2 weeks postimplantation

before settling in the suprachroroidal space. In this study, achieving a stable device position was also dependent on extrinsic factors. Following implantation of the second chronic device, there was a breakdown of the scleral wound. The lead of the epiretinal component was free to move in the wound as it opened, thereby affecting the position of the epiretinal component on the retina. Irrespective of the movement cause by lead force as the scleral wound opened, the components, however, remain coupled across the 5 weeks of implantation suggesting that the magnets have more than one stable pole capable of providing continued attachment under external stress.

It is well established that poor device positioning affects the efficacy of the device (2,19,26). In particular, poor positioning of epiretinal implants have been shown to require higher stimulating currents (25). OCT imaging suggests a misalignment between the curvature of the silicone substrate that forms the device and the retina, and accordingly, the silicone aspects of both devices 1 and 2 led to pressure points and compression of the retina at these points. The superior and inferior OCT scans show that despite the mismatch between the form factor of the epiretinal component and the retinal curvature, the center of the epiretinal component where the electrodes are located is well aligned with the underlying retina, and is separated by a gap of less than 50 μm. Considering that the proposed high-acuity diamond electrode system (20,41–43) that will be used in future testing of the epiretinal implant will have electrodes with a diameter of 125 μm^2, the separation between the electrodes and retina should be less than 125 μm in order to preserve the resolution of the electrodes. Our results suggest this is achievable with the magnetic attachment method. Tacking causes deliberate retinal damage, and the challenge of fixating an epiretinal component to the inner surface of the retina is complicated (44). In both devices used in the current study, the silicone tip caused significant trauma to the retina due to the mismatched shape with the retina and the pressure point this induces at the tip. The implication of this was highlighted by the fluorescein angiogram. The fluorescein angiogram showed that retinal compression occurring at these pressure points limited the ingress of blood flow beneath the epiretinal component. Accordingly, the mismatch in the conformity between the device and the retinal tissue under constant magnet force is an issue of concern. Other contributing factors include the acute movements of the retina during surgery and the displacement of the retina by the pressure exerted by the device. Device placement and stability of our magnetically paired devices were, for the most part reliable, and hence, an amendment to the contour of the silicone substrate to improve conformity with the retina would likely ameliorate the vascular and tissue damage induced by pressure points. Position wise, the electrodes will be temporal to *area centralis*. The location of the epiretinal component is predetermined by the position of the suprachoroidal component as this is the first component surgically implanted, and thus, the electrode array in the epiretinal component will be positioned directly over the location of the suprachoroidal magnet. It is important that the suprachroidal component is positioned as close as possible to *area centralis* as this is the area where the ganglion cells are tightly packed; an electrode array located too far from *area centralis* can result in the unwanted stimulation of retinal ganglion cell axons, leading to imprecise or unexpected percepts (45). The position of the diamond electrodes relative to the underlying retina is the crucial component in the success of this device. Our results suggest that the magnetic coupling between the two components places the electrodes relatively close to the target retinal tissue, near *area centralis*.

Although epiretinal prostheses can be attached to the retina by tacks or glue, this is not suitable to our device design. The EPIRET III device is reportedly <50 μm thick (18,23), while the Argus II is <500 μm (46,47). In comparison, the Bionic Vision Australia epiretinal device, comprising a fully implanted diamond multielectrode (8–11) and diamond capsule to hermetically encapsulate the electronics microchip, is closer to 1 mm thick, and as a result, the tacks need to penetrate through a thick silicone membrane and support 120 mg of mass. Therefore, the requirements for the chosen mechanical fixation technique are considerably more demanding for our device compared with other epiretinal devices. As an alternative, magnets are a resilient and reliable method for epiretinal attachment. Device positioning and stability are paramount for a successful retinal prosthesis fixation method. We have shown that a magnetic attachment strategy is able to safely hold the device in situ for at least 6 weeks. However, it is evident that the longer implantation time causes retinal damage due to the on-going pressure induced under magnet attachment, particularly at the device tip and lead end where the pressure of the magnets appears to be focused. This is indicative of our design strategy in which the diamond electrodes are recessed within the silicone housing, and thus, the retinal tissue beneath does not show the same compressive trauma. However, given that the compression was severe at the epiretinal component tip, it is unlikely that retinal

stimulation at the electrode site will provide any signal pathway to the optic nerve due to ganglion cell axon damage. The gross dissection determined that other damage such as retinal detachment or vitreous hemorrhage did not occur during the study. However, it is clear from OCT imaging of the devices that retinal compression occurred beneath the magnetically coupled devices. Accordingly, the magnets used in this study may require further optimization to their strength in addition to changes in the form factor. Positively, after 6 weeks, we have not seen erosion or amelioration of the retina beneath the magnet. Provided that we can limit the shape mismatch of the device relative to the retinal curvature and reduce the coupling force, in future studies, the magnetic coupling technology appears to be capable of providing a reliable technique to surgically implant an epiretinal prosthesis.

CONCLUSIONS

Force-customized magnets were studied to ascertain the feasibility of their use as a means to attach retinal prostheses. While we believe that magnetic attachment of a retinal prosthesis is a superior methodology to retinal tacking, the long-term success of this technique is dominated by both controllable intrinsic factors (coupling force of the attachment) and also by extrinsic factors (surgical proficiency, lead forces). Here, we have shown that we can routinely control the magnetic flux density of neodymium magnets and provide long-term encapsulation of these magnets to enable their use in vivo. The chronic implantation of a magnetically paired prosthesis requires further optimization. While the forces between the epiretinal and suprachoroidal components were selected to be minimal, the mismatch in device shape relative to the underlying retinal contour led to pressure points through which the magnetic coupling force was driven leading to retinal trauma and severe compression at these locations. The magnetic coupling technique however showed no evidence of any retinal detachment or hemorrhage. The compression of the retinal tissue between the magnets suggests that we have not optimized coupling force; however, we are confident that there is scope within the magnetic coupling technique to further demagnetize the magnets used in our devices to reduce trauma. The magnetic coupling technique provides a number of advantages over the alternative of tacks. Device position was stable across the 6-week implantation period. The distance between the electrodes and the underlying retina is less than 50 μm providing a better outcome than that reported by groups using tacks. Finally, the surgical ease of implementation does not require significant intraocular activity as the devices self-locate. Further investigations will be necessary to optimize the device design and magnetic coupling force; however, we have herein developed a highly promising attachment technique.

Acknowledgments: This research was supported by the Australian Research Council (ARC) through its Special Research Initiative (SRI) in Bionic Vision Science and Technology grant to Bionic Vision Australia (BVA). CERA receives Operational Infrastructure Support from the Victorian Government and is supported by a NHMRC Centre for Clinical Research Excellence Award (#529923). The Bionics Institute acknowledges the support received from the Victorian Government through its Operational Infrastructure Program.

REFERENCES

1. Shepherd RK, Shivdasani MN, Nayagam DA, Williams CE, Blamey PJ. Visual prostheses for the blind. *Trends Biotechnol* 2013;31:562–71.
2. Weiland JD, Cho AK, Humayun M. Retinal prostheses: current clinical results and future needs. *Opthalmol* 2011;118:2227–37.
3. Gerding H, Taneri S, Benner FP, Thelen U, Uhlig CE, Reichelt R. Successful long-term evaluation of intraocular titanium tacks for the mechanical stabilization of posterior segment ocular implants. *Materwiss Werksttech* 2001;32:903–12.
4. de Juan E Jr, Spencer R, Barale P-O, da Cruz L, Neysmith J. Extraction of retinal tacks from subjects implanted with an epiretinal visual prosthesis. *Graefes Arch Clin Exp Ophthalmol* 2013;251:2471–6.
5. Curcio CA, Sloan KR, Kalina RE, Hendrickson AE. Human photoreceptor topography. *J. Comp. Neurol.* 1990;292:497–523.
6. James AL, Daniel SJ, Richmond L, Papsin BC. Skin breakdown over cochlear implants: prevention of a magnet site complication. *J Otolaryngol* 2004;33:151–4.
7. Migirov L, Wolf M. Magnet removal and reinsertion in a cochlear implant recipient undergoing brain MRI. *ORL J Otorhinolaryngol Relat Spec* 2013;75:1–5.
8. Russo A, Shelyakova T, Casino D, et al. A new approach to scaffold fixation by magnetic forces: application to large osteochondral defects. *Med Eng Phys* 2012;34:1287–93.
9. Riley MA, Walmsley AD, Harris IR. Magnets in prosthetic dentistry. *J Prosthet Dent* 2001;86:137–42.
10. Federick DR. A magnetically retained interim maxillary obturator. *J Prosthet Dent* 1976;36:671–5.
11. Ahmad KA, Drummond JL, Graber T, BeGole E. Magnetic strength and corrosion of rare earth magnets. *Am J Orthod Dentofacial Orthop* 2006;130:275, e11–e15.
12. Bondemark L, Kurol J, Wennberg A. Orthodontic rare earth magnets–in vitro assessment of cytotoxicity. *J Orthod* 1994;21:335–41.
13. Fabiano F, Celegato F, Giordano A, et al. Assessment of corrosion resistance of Nd–Fe–B magnets by silanization for orthodontic applications. *Physica B* 2014;435:92–5.
14. Deneuve S, Loundon N, Leboulanger N, Rouillon I, Garabedian EN. Cochlear implant magnet displacement

during magnetic resonance imaging. *Otol Neurotol.* 2008;29:789–90.
15. Sawyer-Glover AM, Shellock FG. Pre-MRI procedure screening: recommendations and safety considerations for biomedical implants and devices. *J Magn Reson Imaging* 2000;12:92–106.
16. Wilson M, Kpendema H, Noar J, Hunt N, Mordan N. Corrosion of intra-oral magnets in the presence and absence of biofilms of *Streptococcus sanguis*. *Biomaterials* 1995;16:721–5.
17. Humayun MS, Dorn JD, da Cruz L, et al. Interim results from the International Trial of Second Sight's Visual Prosthesis. *Ophthalmology* 2012;119:779–88.
18. Roessler G, Laube T, Brockmann C, et al. Implantation and explantation of a wireless epiretinal retina implant device: observations during the EPIRET3 prospective clinical trial. *Invest. Ophthalmol. Vis. Sci.* 2009;50:3003–8.
19. de Balthasar C, Patel S, Roy A, et al. Factors affecting perceptual thresholds in epiretinal prostheses. *Invest. Ophthalmol. Vis. Sci.* 2008;49:2303–14.
20. Hadjinicolaou AE, Leung RT, Garrett DJ, et al. Electrical stimulation of retinal ganglion cells with diamond and the development of an all diamond retinal prosthesis. *Biomaterials* 2012;33:5812–20.
21. Güven D, Weiland JD, Fujii G, et al. Long-term stimulation by active epiretinal implants in normal and RCD1 dogs. *J Neural Eng* 2005;2:s65–s73.
22. Klauke S, Goertz M, Rein S, et al. Stimulation with a wireless intraocular epiretinal implant elicits visual percepts in blind humans: results from stimulation tests during the EPIRET3 prospective clinical trial. *Invest. Ophthalmol. Vis. Sci.* 2011;52:449–55.
23. Laube T, Brockmann C, Roessler G, et al. Development of surgical techniques for implantation of a wireless intraocular epiretinal retina implant in Göttingen minipigs. *Graefes Arch Clin Exp Ophthalmol* 2012;250:51–9.
24. Tunc M, Humayun M, Cheng X, Ratner BD. A reversible thermosensitive adhesive for retinal implants: in vivo experience with plasma-deposited poly (N-isopropyl acrylamide). *Retina* 2008;28:1338–43.
25. Weiland JD, Cho AK, Humayun MS. Retinal prostheses: current clinical results and future needs. *Ophthalmology* 2011;118:2227–37.
26. Ahuja A, Yeoh J, Dorn J, et al. Factors affecting perceptual threshold in Argus II retinal prosthesis subjects. *Transl Vis Sci Technol* 2013;2:1.
27. Xu JL, Huang ZX, Luo JM, Zhong ZC. Effect of titania particles on the microstructure and properties of the epoxy resin coatings on sintered NdFeB permanent magnets. *J Magn Magn Mater.* 2014;355:31–6.
28. Zhang H, Song ZL, Mao SD, Yang HX. Study on the corrosion behavior of NdFeB permanent magnets in nitric acid and oxalic acid solutions with electrochemical techniques. *Mater Corros.* 2011;62:346–51.
29. Zheng J, Jiang L, Chen Q. Electrochemical corrosion behavior of Nd-Fe-B sintered magnets in different acid solutions. *J Rare Earth.* 2006;24:218–22.
30. Opie NL, Ayton LN, Apollo NV, Ganesan K, Guymer RH, Luu CD. Optical coherence tomography-guided retinal prosthesis design: model of degenerated retinal curvature and thickness for patient-specific devices. *Artif Organs* 2014;38:E82–94.
31. Opie NL, Burkitt AN, Meffin H, Grayden DB. Heating of the eye by a retinal prosthesis: modeling, cadaver and in vivo study. *IEEE Trans Biomed Eng* 2012;59:339–45.
32. Villalobos J, Allen PJ, McCombe MF, et al. Development of a surgical approach for a wide-view suprachoroidal retinal prosthesis: evaluation of implantation trauma. *Graefes Arch Clin Exp Ophthalmol* 2012;250:399–407.
33. Saunders AL, Williams CE, Heriot W, et al. Development of a surgical procedure for implantation of a prototype suprachoroidal retinal prosthesis. *Clin. Experiment. Ophthalmol.* 2014;42:665–74.
34. Elvin C, Danon S, Brownlee A, et al. Evaluation of photocrosslinked fibrinogen as a rapid and strong tissue adhesive. *J Biomed Mater Res A* 2010;93:687–95.
35. Nayagam DA, McGowan C, Villalobos J, et al. Techniques for processing eyes implanted with a retinal prosthesis for localized histopathological analysis. *J Vis Exp* 2013; 78:e50411.
36. Alwitry A, Vernon S. *Shared Care Glaucoma*. Chichester: Wiley-Blackwell, 2009.
37. Uhlmann S, Wiedemann P. Refractive lens exchange combined with pars plana vitrectomy to correct high myopia. *Eye* 2006;20:665–70.
38. Villalobos J, Nayagam DA, Allen PJ, et al. A wide-field suprachoroidal retinal prosthesis is stable and well tolerated following chronic implantation. *Invest. Ophthalmol. Vis. Sci.* 2013;54:3751–62.
39. Brandl W, Gendig C. Corrosion behaviour of hybrid coatings. *Thin Solid Films.* 1996;290:343–7.
40. Cieślik M, Engvall K, Pan J, Kotarba A. Silane–parylene coating for improving corrosion resistance of stainless steel 316L implant material. *Corros Sci.* 2011;53:296–301.
41. Ganesan K, Garrett DJ, Ahnood A, et al. An all-diamond, hermetic electrical feedthrough array for a retinal prosthesis. *Biomaterials* 2014;35:908–15.
42. Ahnood A, Escudie MC, Cicione R, et al. Ultrananocrystalline diamond-CMOS device integration route for high acuity retinal prostheses. *Biomed Microdevices* 2015;17:1–11.
43. Lichter SG, Escudié MC, Stacey AD, et al. Hermetic diamond capsules for biomedical implants enabled by gold active braze alloys. *Biomaterials* 2015;53:464–74.
44. Fernandes RAB, Diniz B, Ribeiro R, Humayun M. Artificial vision through neuronal stimulation. *Neurosci Lett* 2012;519: 122–8.
45. Lakhanpal RR, Yanai D, Weiland JD, et al. Advances in the development of visual prostheses. *Curr Opin Ophthalmol* 2003;14:122–7.
46. Kandagor V, Cela CJ, Sanders CA, et al. In situ characterization of stimulating microelectrode arrays: study of an idealized structure based on Argus II retinal implants. In: Zhour DD, Greenbaum E, eds. *Implantable Neural Prostheses 2*. New York: Springer, 2010;139–56.
47. Waschkowski F, Hesse S, Rieck AC, et al. Development of very large electrode arrays for epiretinal stimulation (VLARS). *Biomed Eng Online* 2014;13:11.